

High-Resolution Infrared Imaging of Neptune from the Keck Telescope

S. G. Gibbard

Lawrence Livermore National Laboratory, Livermore, California 94550

E-mail: sgibbard@igpp.ucllnl.org

H. Roe and I. de Pater

Astronomy Department, 601 Campbell Hall, University of California, Berkeley, California 94720

B. Macintosh, D. Gavel, and C. E. Max

Lawrence Livermore National Laboratory, Livermore, California 94550

K. H. Baines

Jet Propulsion Laboratory, Pasadena, California 91109

and

A. Ghez

University of California—Los Angeles, Los Angeles, California 90095

Received May 7, 1999; revised August 20, 2001

We present results of infrared observations of Neptune from the 10-m W. M. Keck I Telescope, using both high-resolution (0.04 arc-second) broadband speckle imaging and conventional imaging with narrowband filters (0.6 arcsec resolution). The speckle data enable us to track the size and shape of infrared-bright features (“storms”) as they move across the disk and to determine rotation periods for latitudes -30 and -45° . The narrowband data are input to a model that allows us to make estimates of Neptune’s stratospheric haze abundance and the size of storm features. We find a haze column density of $\sim 10^6 \text{ cm}^{-2}$ for a haze layer located in the stratosphere, and a lower limit of 10^7 cm^{-2} and an upper limit of 10^9 cm^{-2} for a layer of $0.2 \mu\text{m}$ particles in the troposphere. We also calculate a lower limit of $7 \times 10^6 \text{ km}^2$ for the size of a “storm” feature observed on 13 October 1997. © 2002 Elsevier Science (USA)

Key Words: Neptune; atmosphere; infrared observations.

1. INTRODUCTION

Neptune’s atmosphere is dynamically very active, with maximum wind velocities greater than 400 m/s (Limaye and Sromovsky 1991) and features that change over short time scales. Images taken by Voyager 2 at visible wavelengths show

prominent dark and bright spots on the planet, as well as some bright wispy cloud features (Smith *et al.* 1989). Over the years much time variability in Neptune’s spots has been reported, with time scales varying from hours to years (Ingersoll *et al.* 1995, Baines *et al.* 1995). The most striking observation has been that the Great Dark Spot (GDS) had disappeared when Neptune was re-imaged by the Hubble Space Telescope (HST) in 1994 (Hammel *et al.* 1995).

Resolving Neptune with ground-based imaging is difficult, since the planet’s angular size is only $2.35''$ at mean opposition. The bright companion cloud to the GDS showed up as a diffuse source in conventional images; resolving such features and distinguishing smaller features on the disk requires use of the HST (e.g., Sromovsky *et al.* 2001a, 2001b, 2001c, Hammel and Lockwood 1997, Hammel *et al.* 1995), adaptive optics (Roddier *et al.* 1997, 1998), or speckle imaging (Gibbard *et al.* 1999). In this paper we present diffraction-limited speckle images of Neptune at near-infrared wavelengths taken with the 10-m W. M. Keck I telescope. Our resolution is $0.04''$, corresponding to about 60 resolution elements across the disk of Neptune. This is similar to the resolution of the best HST observations at visible (5000 \AA) wavelengths.

Evidence for weather on Neptune has been available for decades (e.g., Joyce *et al.* 1977, Pilcher 1977, Hammel *et al.* 1989b,

TABLE I

Date	Time (UTC)	Object	Filter	Airmass	Seeing	Phase angle
Sept. 6, 1996	10:42	SAO 188588	Speckle H	1.5		
	11:45	Neptune	Speckle H	1.8		1.43
	12:27	Neptune	KCONT	2.2	0.6''	
	12:31	Neptune	H ₂ 1-0	2.3	0.6''	
	12:35	Neptune	FEII	2.4	0.6''	
	12:40	FS34	FEII	1.8		
	12:44	FS34	H ₂ 1-0	1.8		
	12:46	FS34	KCONT	1.8		
Oct. 10, 1997	4:53	SJ9105-P530	CH ₄	1.5		
	8:32	SAO188682	Speckle H			
	8:45	Neptune	Speckle H	1.5		1.87
	10:35	Neptune	CH ₄	2.4	1.0''	
	10:39	Neptune	H ₂ 1-0	2.5	0.9''	
	10:43	Neptune	FEII	2.6	0.8''	
Oct. 11, 1997	10:47	Neptune	OII		0.9''	
	7:52	SAO188699	Speckle H	1.9		
	8:09	Neptune	Speckle H	2.1		1.87
	9:15	Neptune	CH ₄	3.7	1.8''	
	9:39	SJ9101-P525	CH ₄	1.0		
Oct. 12, 1997	6:15	SAO 188682	Speckle H	1.4		
	7:27	Neptune	Speckle H	1.73		1.88
	8:28	Neptune	CH ₄	2.4	0.8''	
	8:30	Neptune	CH ₄			
Oct. 13, 1997	5:20	Neptune	Speckle H	1.3		1.88
	5:39	SAO188726	Speckle H	1.4		
	6:12	Neptune	CH ₄	1.4	0.6''	
	6:16	Neptune	H ₂ 1-0	1.4	0.45''	
	6:21	Neptune	FEII	1.4	0.6''	
	6:25	Neptune	OII	1.5	0.6''	
	6:42	SJ9182	CH ₄	1.2		
	6:44	SJ9182	H ₂ 1-0	1.2		
	6:48	SJ9182	FEII			
	6:52	SJ9182	OII			

Lockwood *et al.* 1991, Hammel *et al.* 1992). Observations of Neptune at visible wavelengths probe cloud layers in the planet's troposphere (at pressure $P \gtrsim 0.1$ bar), whereas observations at infrared wavelengths, where methane gas is the main source of opacity, are primarily sensitive to features in Neptune's stratosphere and upper troposphere. An infrared-bright feature accompanied the Great Dark Spot imaged by Voyager 2 (Smith *et al.* 1989). It is not known, however, if infrared-bright features are typically associated with disturbances in the troposphere such as the GDS.

In order to investigate features of Neptune seen at near-infrared wavelengths and to model the planet's stratospheric haze, we have observed Neptune from the 10-m W. M. Keck I Telescope, using both high-resolution (0.04'') broadband speckle imaging and conventional imaging with narrow-band filters (0.6'' resolution). The speckle data enable us to track the size and shape of infrared-bright features, and to determine rotation periods for latitudes where bright features occur. The narrowband data allow us to make estimates of Neptune's stratospheric haze abundance.

2. OBSERVATIONS AND DATA REDUCTION

We observed Neptune with the 10-m W. M. Keck I telescope¹ on Mauna Kea, Hawaii, on September 6, 1996 (UT) and October 10–13, 1997 (UT). During these times Neptune's sub-Earth latitude (planetographic) was -25° , so that our images show primarily Neptune's southern hemisphere. Table I summarizes dates, times, and wavelengths of these Neptune observations.

We observed Neptune both in speckle imaging mode (see below) and using conventional observing techniques (we refer to the latter as narrowband images). For both types of observations we used the facility's near-infrared camera (NIRC; Matthews and Soifer 1994), which is equipped with a 256×256 pixel Santa Barbara Research Corporation InSb array. The pixel size is 0.151''. For speckle observations a plate scale changer is inserted into the light path to produce a scale of 0.0203'' per pixel

¹ The Keck telescope is jointly owned and operated by the University of California and the California Institute of Technology.

TABLE II
Filter Characteristics

Filter name	Central wavelength (μm)	Wavelength range (μm)
OII	1.236	1.231–1.241
FEII	1.647	1.638–1.656
H	1.658	1.491–1.824
H ₂ 1-0	2.125	2.113–2.137
KCONT	2.260	2.233–2.286
CH ₄	2.269	2.192–2.347

(Matthews *et al.* 1995), well-matched to the telescope’s 2- μm diffraction limit (0.04”). Table I shows the list of narrowband images and reference stars for each night. A typical angular resolution for these observations is $\sim 0.6''$. The conventional images were taken at several different wavelengths between 1 and 3 μm in order to probe different altitudes in Neptune’s stratosphere. The filters used are shown in Table II.² They will be referred to by the central wavelength shown in the table. The narrowband data were processed by correcting for bias and saturation, removing bad pixels, flat-fielding, and sky subtracting. In the wide-field images signal to noise is extremely high, 25 to 40:1 in the dimmest pixels on the planet in the longer-wavelength filters (2.21 and 2.27 μm), and 1000:1 in the short-wavelength images (1.24 and 1.65 μm). Photometric calibration errors are dominated by uncertainties in the airmass correction at these wavelengths and the brightness of the standard stars at these wavelengths, conservatively estimated at 10%, although the standard is a G spectral type and should have little spectral variation in the near-IR.

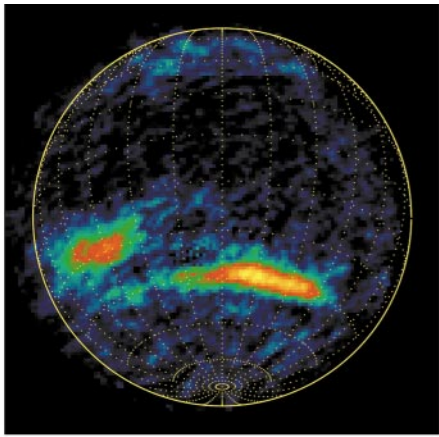
Speckle imaging is a technique in which many very short exposures (typically 300 milliseconds for the Neptune observations) are taken to “freeze” telluric atmospheric turbulence and capture the light while it is still forming coherent interference patterns at the detector. The coherence patterns contain diffraction-limited information that can subsequently be used to determine the object’s Fourier amplitudes and phases, which are combined with an inverse Fourier transform to produce a diffraction-limited image. The data were preprocessed as conventional infrared images before the speckle analysis procedure. The instrument dark current and (time-varying) bias were removed using bias frame stacks associated with each data set. Data were sky-subtracted using 300-frame blank-sky observations taken shortly before or after the Neptune and reference star images. A median filtering technique was then applied to each image to remove residual columnar patterns caused by drifts in the instrument electronics. The resulting images were flat-fielded using flats constructed from twilight sky images. The data were then postprocessed using the power spectrum and bispectrum speckle image reconstruction algorithms (for details of this process, see Gibbard *et al.* 1999).

Our speckle images are typically taken as stacks of 100 exposures. The stacks are combined into a single image using the speckle techniques described above. Each of these images is then rotated so that sky north is up, and added to other speckle processed images to produce the final image of Neptune (typically such an image will be made from 400–800 300-ms exposures). Due to the rotation of Neptune, the final image is blurred in longitude by approximately 3° on the planet at the equator, or 3.5 at -45° during the ~ 10 -min time interval between the first and last image frames.

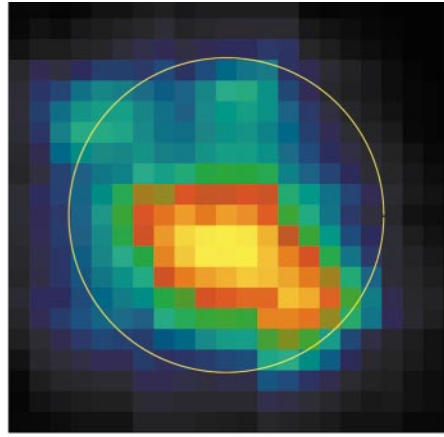
Both speckle and narrowband images from September 6, 1996, and October 10–13, 1997, are shown in Figs. 1–5. Figure 1 shows the speckle H band image and the three narrowband images obtained on September 6, 1996, and Figs. 2–5 show speckle and narrowband images from October 10–13, 1997. Actual pixels are shown, without interpolation; however, the narrowband images shown for October 13 have been deconvolved as described below.

Among the narrowband images, the October 13 images have the best angular resolution (Table I), and we attempted to enhance this resolution by applying the Lucy–Richardson deconvolution algorithm, using Triton (also present in the images and, at 0.125”, unresolved) as a PSF reference. As a test of the limitations of this deconvolution procedure we constructed a model image of Neptune in the 1.65- μm filter (using the model discussed in Section 4), adding to the clear atmosphere model two “storm” features and a polar hood similar to those seen in the data. The storms and the polar hood were modeled with a total flux (hood + storms) equal to the difference between our actual data and the model; in this way the model plus the storms and polar hood had the same flux as our data. The relative flux of the storms and polar hood was determined by the relative values of these features in the original data. The flux ratios determined were then: clear atmosphere 30%, storm 1 (on the right of the disk in Fig. 6) 34%, storm 2 23%, and polar hood 11%. We then convolved this model with Triton and sampled it down by a factor of 3 to the coarser grid size of our actual data. We added noise equal to the read noise plus Poisson sky noise in our original image. We then deconvolved this artificial image using the Lucy–Richardson deconvolution algorithm and a varying number of iterations. We find that 50–100 iterations give a good fit to the original data; further iterations simply add noise at high spatial frequencies (not apparent in the row averages shown in Fig. 6d), although they do not significantly change the average flux (Fig. 6b). The data analyzed in this paper were deconvolved using 80 iterations. Although some ringing can be seen in Figs. 6c and 6d, this does not affect the row average photometry near the center of the image, which is the quantity we are attempting to fit with our models. This modeling allowed us to be confident in the results of our deconvolution of the October 13 data. We estimate that deconvolution adds an error of 10–20% to our overall I/F values; thus our total estimated error in I/F (including photometry errors discussed above) is about $\pm 20\%$.

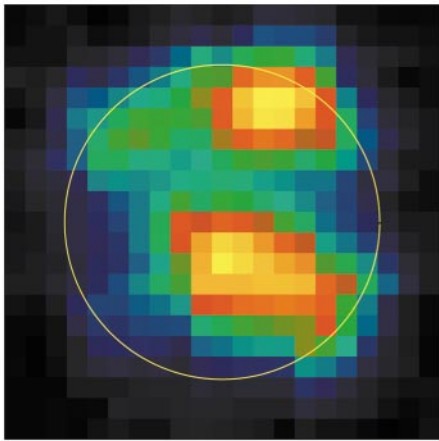
² Filter traces can be found at the Keck Observatory website, <http://www2.keck.hawaii.edu:3636/>



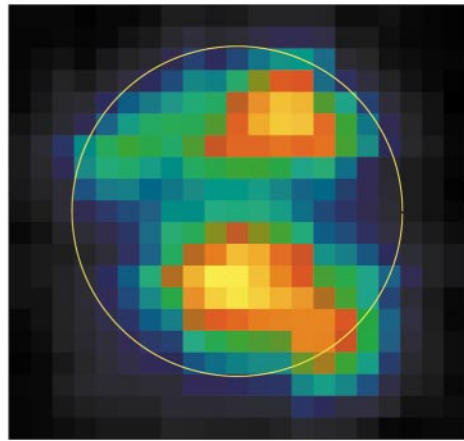
1a. Sept 6 1996 H band speckle



1b. Sept 6 96 1.65 microns (FEII)



1c. Sept 6 96 2.12 microns (H2 1-0)



1d. Sept 6 96 2.26 microns (KCONT)

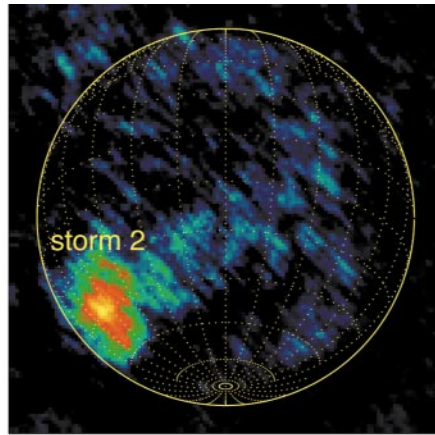


FIG. 1. Images of Neptune from September 6, 1996. The sub-Earth latitude is -25° ; north is up. (a) H-band speckle image, (b) $1.65 \mu\text{m}$, (c) $2.12 \mu\text{m}$, (d) $2.26 \mu\text{m}$. The circles in Figs. 1–5 indicate the approximate location of the planetary limb. The circles are located such that the bright limbs (especially visible in the northern hemisphere) and all infrared-bright features (but not necessarily the scattered light from these features) are within the limb. The colorbar shows the relative intensity of different parts of the planet, with the maximum intensity being 1.

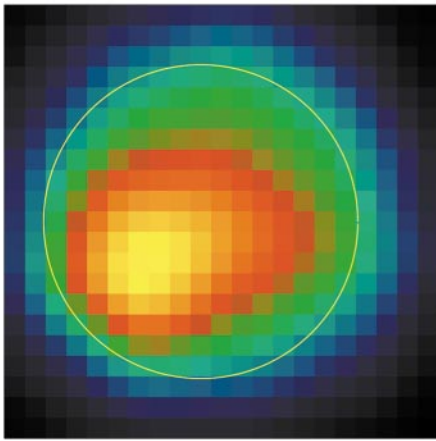
3. SPOT ROTATION PERIODS

In the October 1997 speckle data we see bright spots at the same latitude on different days, and hence are able to calculate rotation periods for these features, assuming that they do not evolve significantly from night to night (although rapid evolution

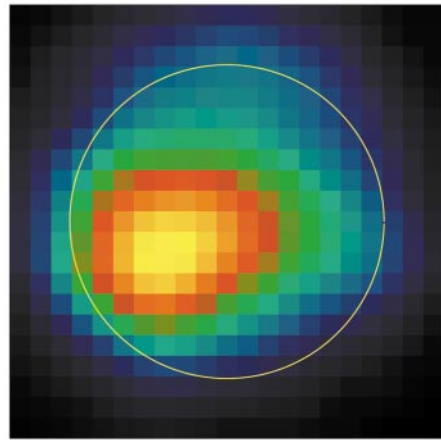
can occur; Limaye and Sromovsky 1991). We observed a bright feature at -45° on October 10, 11, and 13 (this feature is just coming onto the limb in the image from October 12; Fig. 4); on October 11 and 12 there is a feature at -30° . These features have been labeled in Figs. 2–5 (Storm 1 is the feature at -30° , and Storm 2 the feature at -45°). In order to find rotation periods,



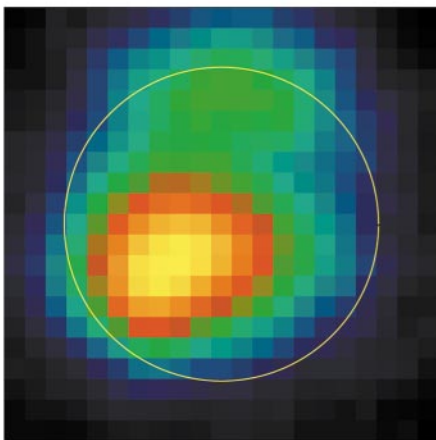
2a. Oct 10 97 H band speckle



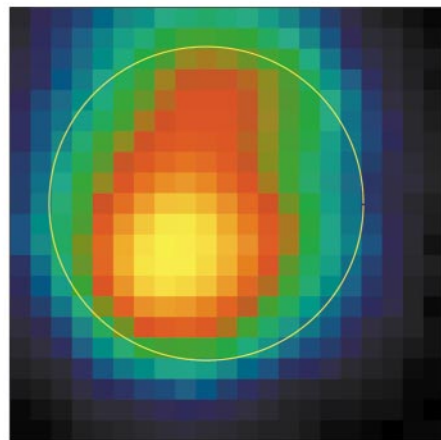
2b. Oct 10 97 1.24 microns (OII)



2c. Oct 10 97 1.65 microns (FEII)



2d. Oct 10 97 2.12 microns (H2 1-0)



2e. Oct 10 97 2.27 microns (CH4)

FIG. 2. Images of Neptune from October 10, 1997. (a) H-band speckle image, (b) 1.24 μm , (c) 1.65 μm , (d) 2.12 μm , (e) 2.27 μm . Colorbar is shown in Fig. 1.

the image from each date was projected onto a latitude–longitude grid, and the leading edge, center, and trailing edge of the spots were identified. Then a rotation period was calculated from the movement in longitude of the spots over the observation interval ($\simeq 23$ hours). The rotation period was taken as the average of the movement of the leading edge, center, and trailing edge (since these spots may change shape over time, it is difficult to know which measurement is the most accurate). Two sources of error identified were in locating the center of the disk of Neptune and in pinpointing the edges of the bright features. We estimate this error as ± 3 pixels per image, which gives a root mean square error of 8.5° for the difference in spot location from night to night.

The rotation periods we find are 17.1 ± 0.3 hours for the spot at $-45 \pm 8.5^\circ$ and 17.8 ± 0.3 hours at $-30 \pm 8.5^\circ$. These can be compared with values reported in the literature (Fig. 7). Both values agree well with previously reported bright feature rotation periods and with a curve fit to Neptune’s rotation rate by Sromovsky *et al.* (1993).

4. MODELING NEPTUNE’S STRATOSPHERE

We observed Neptune in narrowband filters to extract information about the vertical structure of Neptune’s cloud features and haze layers. These narrowbands vary in degree of sensitivity to absorption by methane and hydrogen gas and therefore probe different altitudes in Neptune’s atmosphere (as shown in Fig. 8). The shortest wavelength filter, $1.24 \mu\text{m}$, is the least sensitive to methane and hydrogen absorption, and thus probes into the troposphere, but not as deep as the cloud layer at $3.5\text{--}4.5$ bars. The $1.65\text{-}\mu\text{m}$ filter is sensitive to the CH_4 haze layer in the troposphere, but not to the lower tropospheric cloud layers. The $2.12\text{-}\mu\text{m}$ filter is dominated by hydrogen, rather than methane, absorption. Both this filter and the $2.27\text{-}\mu\text{m}$ filter, which is centered on a strong methane absorption band, sample the atmosphere down to the lower stratosphere, just above the tropopause.

In order to compare the narrowband images among themselves and with models we calculated the I/F (ratio of reflected intensity to solar flux) for the images, as described in Hammel *et al.* (1989a). For September 6, 1996, the data were calibrated using the UKIRT photometric standard star FS34 (aka EG141, Cassali 1992). For October 13, 1997, the standard photometric star SJ9182 (Persson *et al.* 1998) was used to calibrate the intensity of the data. Solar flux values were taken from Colina *et al.* (1996). The data from October 13 have been deconvolved as described in Section 2. As a check on the accuracy of our photometric calibration, we calculated values for the albedo of Triton, which appears in our narrowband images (but is saturated in the $2.27\text{-}\mu\text{m}$ filter). Table III shows the values obtained for the average I/F (which, for the small phase angles considered here is close to the geometric albedo) of Neptune and Triton in each filter. Our values for the average I/F of Triton, within our margin of error of $\pm 20\%$, are in agreement with the H-band values found by Sromovsky *et al.* (2001b).

TABLE III
Average I/F of Neptune and Triton

Object	Wavelength (μm)	Avg. I/F
Neptune	1.236 (OII)	0.010 ± 0.002
Neptune	1.647 (FEII)	0.0046 ± 0.0009
Neptune	2.125 (H_2 1-0)	0.0014 ± 0.0003
Neptune	2.269 (CH_4)	0.0016 ± 0.0003
Neptune	1.658 (H)	0.012 ± 0.0024
Triton	1.236 (OII)	0.75 ± 0.16
Triton	1.647 (FEII)	0.59 ± 0.12
Triton	2.125 (H_2 1-0)	$0.70 \pm .14$
Triton	2.269 (CH_4)	***
Triton	1.658 (H)	0.65 ± 0.14

*** Saturated.

The average I/F of Neptune appears to be considerably lower than the values found by Fink and Larson (1979), a result that was also noted by Sromovsky *et al.* (2001b). However, we note that the Fink and Larson spectra for Neptune are at low resolution ($46/\text{cm}$), and that the data for the $2\text{--}2.5 \mu\text{m}$ region appear to be at the noise level. Therefore, we cannot make a meaningful comparison between their results and our 2.12- and $2.24\text{-}\mu\text{m}$ filter values. Our data at 1.24 and $1.65 \mu\text{m}$ are approximately a factor of 5 lower than the Fink and Larson values at the same wavelengths, although the lack of errors bars in their data makes it difficult to determine the significance of this. An actual large change in the average I/F of Neptune is perfectly plausible (as was suggested by Sromovsky *et al.* (2001b)), since the infrared light from the planet is dominated by highly variable bright features.

We have chosen to model the narrowband data of October 13 (Fig. 5); on this day we obtained the highest resolution ($0.6''$) conventional images, which we deconvolved using a Lucy–Richardson algorithm (described in Section 2) to obtain a resolution high enough to clearly separate the spots (“storms”) from spot-free regions (“quiescent atmosphere”). The clouds generally tend to be aligned longitudinally; latitudes near -10° seemed typically to be storm-free and were used to determine our nominal quiescent atmosphere model. Neptune is modeled on a grid with a spacing of 0.05 fractional planet radii, which translates into $0.058''$ or 2.6 grid points per NIRC-pixel (a NIRC pixel being $0.15''$). Figure 9a shows one of the images ($2.12 \mu\text{m}$) with a longitude–latitude grid superposed; the scan is superposed as +signs, one symbol at each “gridpoint.” Because the scans are along curved lines, the data points on the +signs are interpolated. Models were convolved with a Gaussian of 2 NIRC-pixels FWHM (full width at half power), so that the model and data have the same spatial resolution.

Figure 9 shows scans through the four different wavelengths both through the quiescent atmosphere at -10° (Fig. 9b) and through a “storm” -45° (Fig. 9c) in units of I/F. Note that our model fits will not attempt to match the *shape* of these curves; the models are instead fit to the *average* values of I/F across the clear atmosphere slices.

We used a model atmosphere program from Baines and Hammel (1994; hereafter referred to as BH1994) to model the low-resolution multiwavelength images. We updated the BH1994 program with the atmospheric temperature–pressure curve from Lindal (1992), and extended it up to higher altitudes (0.025 mbar) than used by BH1994. Using a profile that is warmer at very low pressures (e.g., Orton *et al.* 1992 as used in Moses *et al.* 1995), has a negligible effect on the model. For our nominal model we adopted a CH₄ fractional abundance of 0.022 in the troposphere (Baines *et al.* 1995), and 0.00035 in the stratosphere (BH1994). Wherever the tropospheric or stratospheric number exceeds saturation, the methane abundance follows the saturated vapor curve. Photochemistry models predict the formation of hydrocarbons in the stratosphere, such as C₂H₂, C₂H₆, C₄H₂, HCN, C₃H₈, C₃H₆ (e.g., Romani and Atreya 1989, Romani *et al.* 1993), decreasing the CH₄ abundance in the stratosphere below the saturated vapor curve; i.e., our value for the CH₄ mixing ratio is below the saturation value throughout the upper (warmer) part of the stratosphere, and this number is expected to decrease further with increasing altitude.

As in BH1994, we used spherical particles with radii of 0.2 μm for the stratospheric haze. We adopted their parameters to characterize the particles and scattering behavior (i.e., single scattering albedo $\varpi \approx 1$, imaginary index of refraction $n_i = 0$, the real indices of refraction 1.44, and a log-normal particle distribution with $\sigma = 1.35$). Wavelength dependences were calculated assuming Mie scattering. In the troposphere we place an optically thick layer at pressures $P \gtrsim 3.8$ bars (presumably the H₂S cloud, as expected from thermodynamic calculations; de Pater *et al.* 1991)). None of the narrowband filters we used is sensitive to the properties of this cloud.

We have further updated the BH1994 model to include more recent H₂ collision-induced absorption coefficients. These coefficients are generated by code described in Borysow (1991, 1993) (for H₂ – H₂ 1-0), Zheng and Borysow 1995 (H₂ – H₂ 2-0), and Borysow *et al.* (1989), and Borysow and Frommhold (1989) for H₂ – He 1-0 and 2-0.

The structure of the haze layers used in BH1994 is relatively complex, involving three stratospheric layers and two tropospheric layers. While the vertical haze structure of Neptune’s atmosphere is probably quite complex, with several distinct layers (Moses *et al.* 1992), in order to reduce the number of parameters in our model we first model Neptune’s haze as a single layer, with varying altitude and number density. We then investigate a haze structure with both a stratospheric and a tropospheric haze layer. While one can envision a continuous haze layer stretching from the stratosphere down into the troposphere that could simultaneously fit all our data, as suggested by the model presented in Moses *et al.* (1995), in order to gain some better understanding of the particle number densities implied by our data and model, we will limit ourselves to no more than two haze layers, one in the stratosphere and one in the troposphere.

In a series of models we first place a single haze layer, thin compared to the scale height of the atmosphere, at different pres-

sure levels in the atmosphere. For each case of haze layer altitude we calculate the column density (#cm⁻²) of haze particles that is necessary to match the observed average I/F (averaged across a slice at -10° as shown in Fig. 9a). The averaging procedure consists of summing all the (sampled) pixels of the slice and then dividing by the number of pixels that overlapped the actual disk. Figure 10 shows the results for each of the four filters, along with $\pm 20\%$ error bars.

We first note that all four filters could be fit by a single haze layer at roughly 0.3 bar of column density $\sim 10^7$ cm⁻². However, such a haze layer seems unlikely based on what is known of the structure of Neptune’s atmosphere (e.g., Baines *et al.* 1995). Another solution, which we find more plausible, is a haze layer of $\sim 10^6$ cm⁻² ($3 \times 10^5 - 2 \times 10^6$ cm⁻²) above ~ 0.05 bar to satisfy the 2.12- and 2.27- μm data. This layer can be distributed and need not be a thin layer. To satisfy the 1.24- and 1.65- μm data we require another haze layer at a pressure greater than roughly 0.6 bar. An example of such a deeper layer that fits both 1.24 and 1.65- μm would be a thin layer of 0.2 μm (radius) particles at a column density of 5×10^7 cm⁻² at 0.9 bar. This tropospheric layer must have at a minimum the equivalent of 10^7 cm⁻² (this number is what is required for the case of a thin layer at ~ 0.7 bar, just below the level to which the 2.27/2.12- μm data probe). If this tropospheric layer lies at a higher pressure or is extended more deeply (both quite likely), then the required column density is higher; we can place an upper limit on its value by considering a haze layer at the methane supersaturation level of ~ 1.4 bars; the required haze column density would be $\simeq 10^9$ cm⁻².

The optical depths that would result from a stratospheric layer of particles of column density 10^6 cm⁻² are shown in Table IV; these numbers can easily be scaled to any column density since they are linearly dependent on this number.

We note again that the results shown here are calculated so as to match the average brightness of the planet; no attempt is made to match limb brightening or the shape of the planet’s limbs. Our results depend on the assumed values of several different quantities. Since we use the significant variation in methane absorption across our filter set to probe different altitudes in Neptune’s stratosphere, it is crucial to have an accurate model to represent methane absorption as a function of wavelength. The BH1994 program was updated to utilize an accurate representation of the methane absorption bands, through the use of k -distribution coefficients. Two sets of methane self-broadened coefficients have

TABLE IV
Optical Depths for a Stratospheric Haze Layer of Column
Density $10^6/\text{cm}^2$

Filter name	Central wavelength (μm)	Optical depth
OII	1.236	2.3×10^{-4}
FEII	1.647	7.6×10^{-5}
H ₂ 1-0	2.125	2.9×10^{-5}
CH ₄	2.269	2.2×10^{-5}

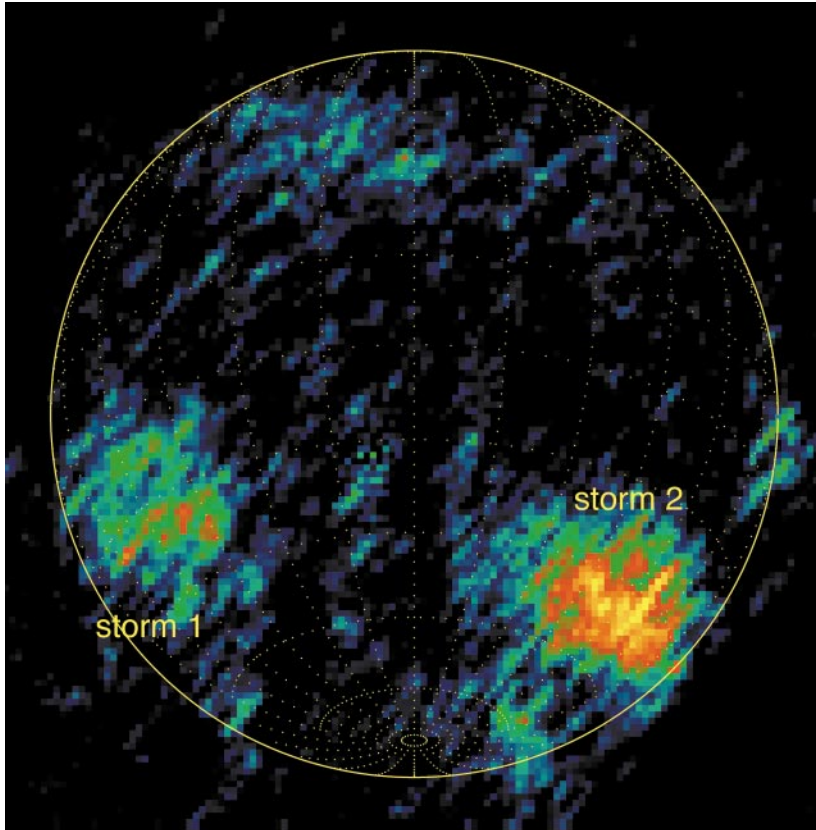


FIG. 3. H-band speckle image of Neptune from October 11, 1997. Colorbar is shown in Fig. 1.

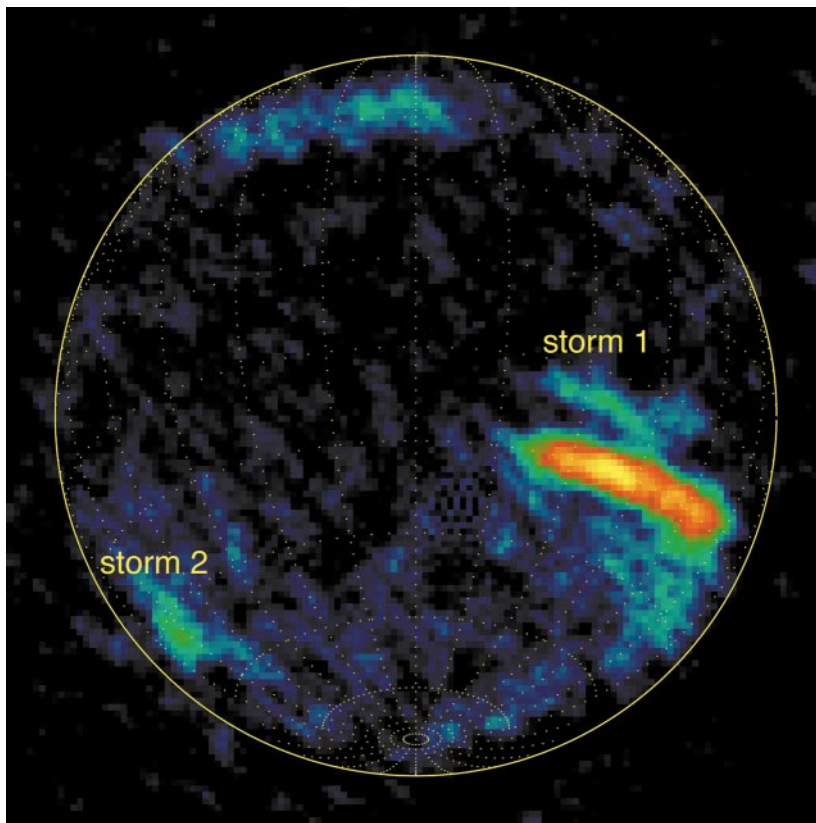
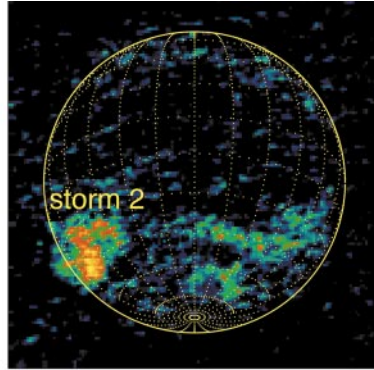
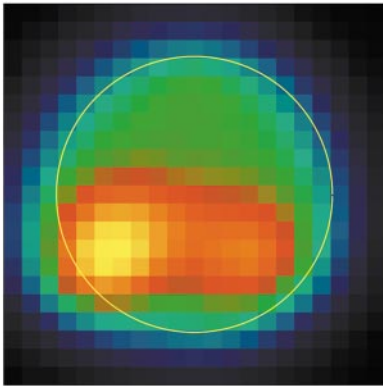


FIG. 4. H-band speckle image of Neptune from October 12, 1997. Colorbar is shown in Fig. 1.

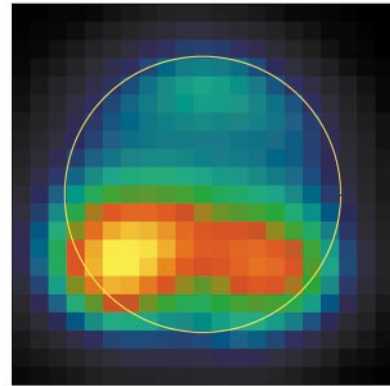


5a. Oct 13 97 H band speckle



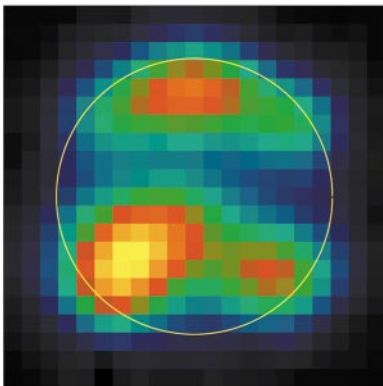
5b. Oct 13 97 I/F 1.24 microns (OII)

0.00 0.002 0.004 0.006 0.008



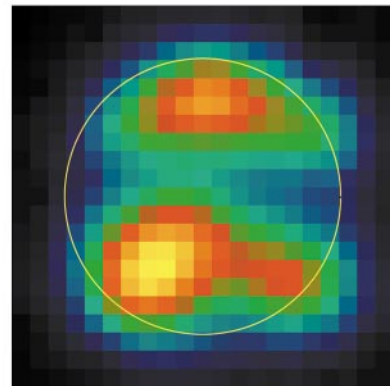
5c. Oct 13 97 I/F 1.65 microns (FeII)

0.00 0.0014 0.0028 0.0042 0.0056



5d. Oct 13 97 I/F 2.12 microns (H2 1-0)

0.00 0.00055 0.0011 0.00165 0.0022



5e. Oct 13 97 I/F 2.27 microns (CH4)

0.00 0.00025 0.0005 0.00075 0.001



FIG. 5. Images of Neptune from October 13, 1997, deconvolved using a Lucy–Richardson algorithm, 80 iterations with Triton used as a reference point source. Shown are a speckle H-band image (5a), and four narrowband images (5b–5e). These are the images used for the modeling discussed in Section 3. Colorbar shows the I/F for each image.

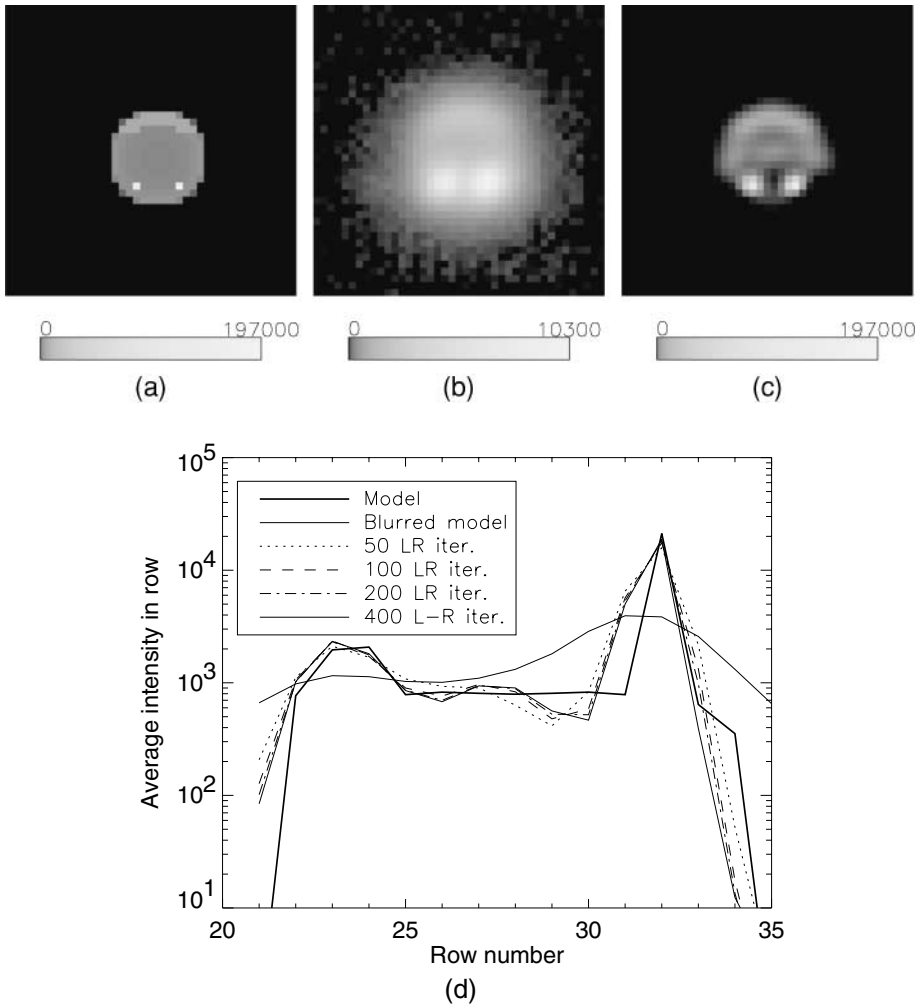


FIG. 6. Test of the deconvolution algorithm applied to a model with artificial “storm” features (for details see text). (6a) Model of 1.65- μm data, with two bright single-pixel storm features added in the southern hemisphere and a polar hood. (6b) The same model, convolved with a PSF source (Triton), with noise added equal to the read noise and Poisson sky noise in the original image. Note the different maximum value on the scale bar. (6c) Deconvolution of the model shown in Fig. 6b; 80 iterations. (6d) Slices through the model shown in Figs. 6a–6c, showing the effect of varying numbers of iterations of a Lucy–Richardson deconvolution algorithm.

been published (Baines *et al.* 1993: wavelength range 1.60–2.52 μm ; Irwin *et al.* 1996: wavelength range 1.05–5.0 μm), and one set of H_2 -broadened coefficients (Irwin *et al.* 1996). Differences in the self-broadened coefficients lead to noticeable differences in the modeled brightness only in the 1.65- μm filter. In the 1.24- μm filter we have only values from Irwin *et al.*, while in the 2.12- μm and 2.27- μm filters the difference in modeled brightness based upon the two sets of coefficients is small. Since it is most appropriate to use the H_2 -broadened coefficients in a hydrogen-dominated atmosphere such as Neptune’s, we use these in all calculations here.

Another important consideration is the equilibrium (H_2E) versus normal (H_2N) distribution of ortho/para hydrogen. H_2E versus H_2N is important only for temperatures less than about 150 K (above this temperature the distributions are almost identical). The difference between the two distributions becomes

significant at $\simeq 100$ K. Because of the difficulty in converting H_2 ortho to H_2 para, there is reason to believe that the actual distribution may lie somewhere between H_2E and H_2N (Massie and Hunten 1982). We find that changing from H_2E to H_2N does not make a significant difference for any filter; the largest difference occurs in the 1.24- μm filter where the difference is at most a few percent. The equilibrium distribution is used in all calculations discussed here.

Our results are also dependent on the values of the stratospheric and tropospheric methane abundance. As discussed above, we have chosen not to vary the methane abundance in our model since the uncertainties in our data are large enough that we cannot provide new constraints on these abundances. If we could reduce the photometric uncertainty in all images to an insignificant level we could, in theory, constrain the methane abundance. However, considering the uncertainty in methane k-coefficients (Baines

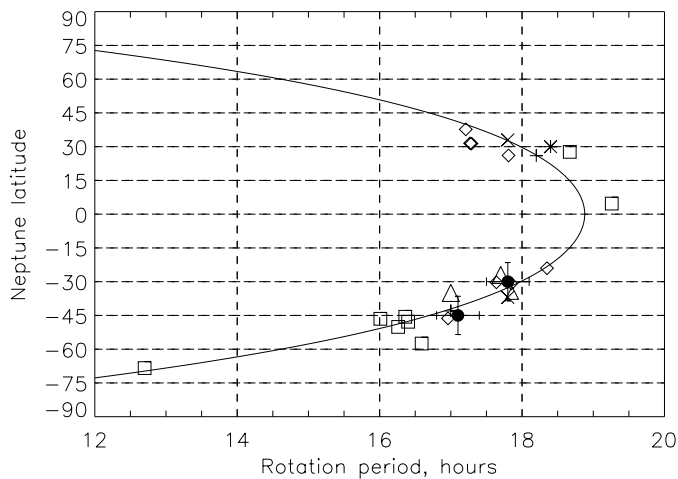


FIG. 7. Rotation periods of Neptune at various latitudes as determined by tracking of cloud features. Dark circles: this work. Plus signs: Roddier *et al.* (1998). Stars: Hammel *et al.* (1995). Squares: Sromovsky *et al.* (1995). Diamonds: Hammel and Lockwood (1997). Small triangles: Hammel and Buie (1987). Large triangles: Hammel *et al.* (1989b). X's: Belton and Terrile (1984). Solid line is fit to Voyager data by Sromovsky *et al.* (1993).

et al. 1993, Irwin *et al.* 1996), which are based on lab spectra at significantly warmer temperatures, we feel that an attempt to independently determine the methane abundance from our data is not warranted.

Our value for the stratospheric haze column density is not significantly different from the value derived by BH1994, (nominal value 8.3×10^6 , range of uncertainty $2\text{--}17 \times 10^6 \text{ cm}^{-2}$). We

note that BH1994 analyzed data taken between 0.6 and $0.9 \mu\text{m}$; these data are thus sensitive to particles larger than $\sim 0.2 \mu\text{m}$ in diameter (from Mie theory, at smaller sizes the extinction efficiency decreases quickly), while these smallest particles are nearly transparent at the infrared wavelengths we observe. It is possible that the tropospheric haze is made up of a bimodal particle distribution, or that the particles display a distribution in size, such that the clouds are more opaque at visible than at infrared wavelengths (this is analogous to the clouds seen on Jupiter; e.g., West *et al.* 1986).

Our calculated value for the stratospheric haze column density is well below the maximum calculated by Romani *et al.* (1993) based upon the hydrocarbon photochemistry ($\sim 2 \times 10^8 \text{ cm}^{-2}$). Pryor *et al.* (1992) derived a value of $2.5 \times 10^7 \text{ cm}^{-2}$ – $6.2 \times 10^7 \text{ cm}^{-2}$ from the Voyager PPS data, using $0.2\text{-}\mu\text{m}$ particles with an imaginary index of refraction $n_i = 0.03$. However, their data were averaged over all longitudes at the latitude bin -20 to -30° ; in our data these latitude bins are contaminated by storm systems, and it is conceivable that the Voyager numbers did, in part, result from enhanced stratospheric hazes.

Storms

Our images (Figs. 1–5) show several clouds or storms in Neptune's atmosphere. From the speckle data shown in Fig. 5 we estimate the maximum size of the storm on October 13 to be roughly $3 \times 10^7 \text{ km}^2$; the brighter central region is about 10^7 km^2 . The clouds are clearly aligned with latitude circles. We modeled the storm as an elongated cloud at latitude -45° . This storm is superposed on the storm-free atmosphere model

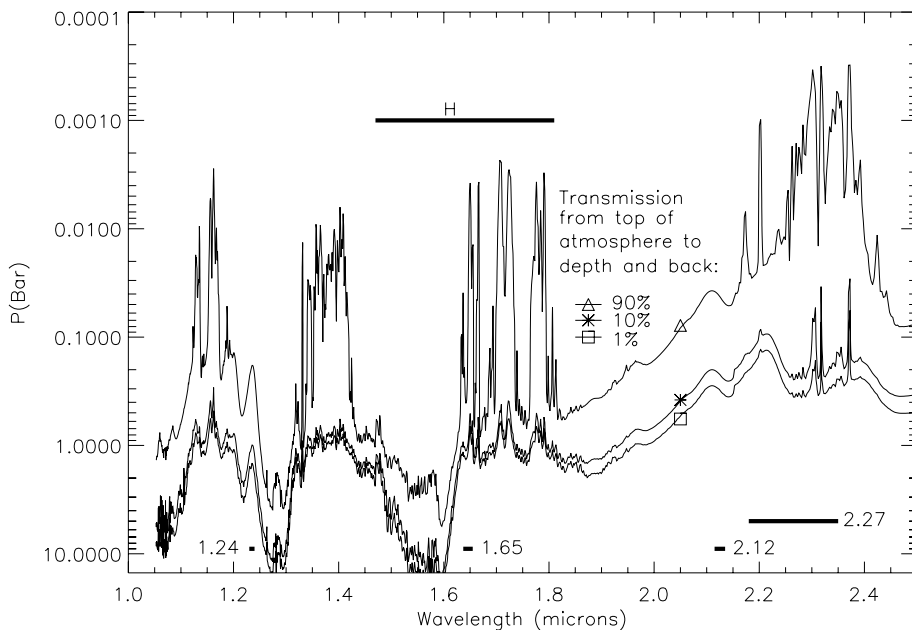


FIG. 8. Transmission along the local vertical in Neptune's atmosphere at infrared wavelengths from 1 to $2.5 \mu\text{m}$, averaged over 5 cm^{-1} bins. Only contributions by hydrogen and methane are included in the opacity. The curves show pressure levels at which 1%, 10%, and 90% of the light is transmitted from the top of the atmosphere to the given pressure level and back. Methane fractional abundance is assumed to be 0.022 in the troposphere and 0.00035 in the stratosphere. The wavelength ranges of the narrowband filters and the broadband H filter discussed in this work are shown.

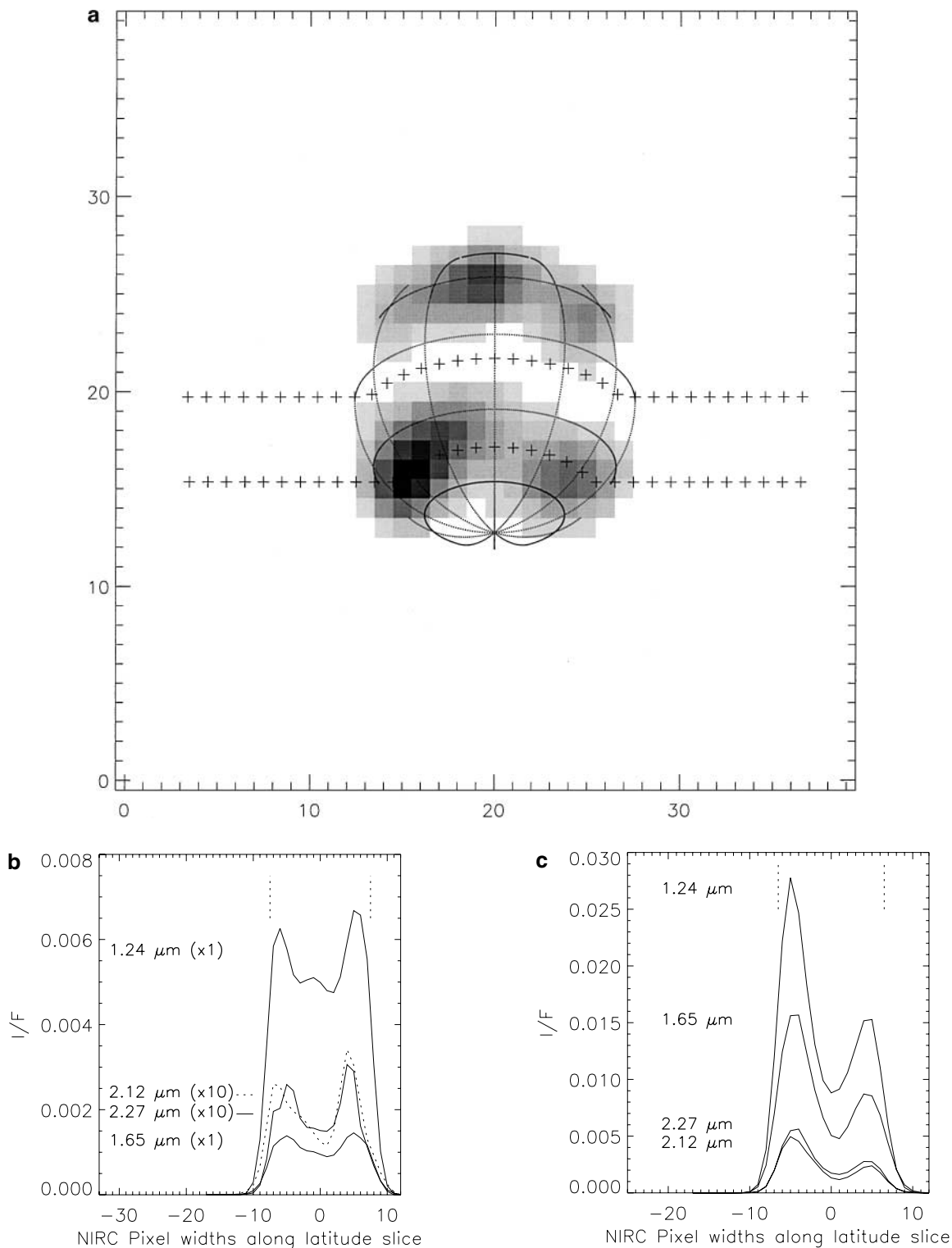


FIG. 9. (a) The 2.12- μm image taken at 6:16 on October 13, 1997 (UT) with the location of the storm-free-atmosphere scan (-10°) and the storm scan (-45°) superposed. (b) Scans of I/F through the storm-free atmosphere at -10° in all four narrowband filters (1.24, 1.65, 2.12, and 2.27 μm). The 2.12- and 2.27- μm filter values have been multiplied by a factor of 10 for clarity. Errors in the I/F are, as indicated in the text, $\pm 20\%$. (c) Scans of I/F through the storm at -45° in all four narrowband filters (1.24, 1.65, 2.12, and 2.27 μm).

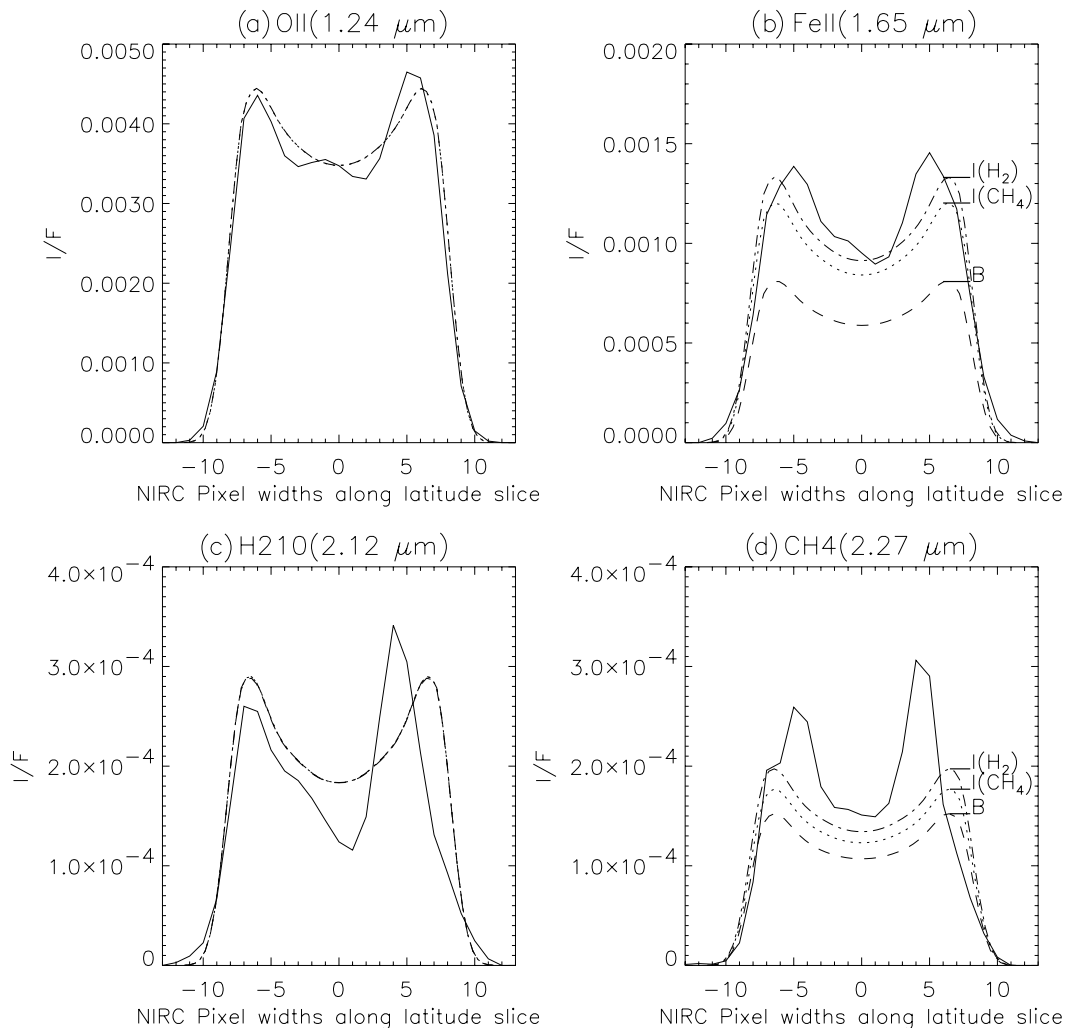


FIG. 10. Best fit haze column density vs. pressure level for a single layer of $0.2\text{-}\mu\text{m}$ particles. Densities are calculated based on the observed I/F for each of the narrowband filters. In the stratosphere the density is determined by the 2.27- and $2.12\text{-}\mu\text{m}$ filters, which are sensitive to the haze density at this pressure level (Fig. 8). Abundances in the upper troposphere are constrained by the 1.24- and $1.65\text{-}\mu\text{m}$ filters. The magnitude of the error bars is shown by the vertical lines; the size of these error bars remains roughly constant as a function of log pressure.

derived above; to determine the storm brightness the background light is subtracted. To find a hard lower limit on the storm size we set the I/F at each wavelength equal to unity in the storm; i.e., we assume a perfectly reflecting layer. To match the observed storm brightness with such a layer requires a storm size $\geq 7 \times 10^6 \text{ km}^2$ at $1.24 \mu\text{m}$, $\geq 4 \times 10^6 \text{ km}^2$ at $1.65 \mu\text{m}$, $\geq 1 \times 10^6 \text{ km}^2$ at 2.12 , and $\geq 1.5 \times 10^{-6} \text{ km}^2$ at $2.27 \mu\text{m}$.

With the data we have it is difficult to tell the exact size of the storm feature we observed on October 13. Our speckle image gives a maximum value of about $3 \times 10^7 \text{ km}^2$ (because of scattered light from the storm the actual size is certainly smaller). For comparison, the Great Dark Spot had a size of $30\text{--}45^\circ$ in longitude and $12\text{--}17^\circ$ in latitude (with the shape changing over time; Ingersoll *et al.* 1995), for an area of about $7.4 \times 10^7 \text{ km}^2$ (taking the average of these longitude and latitude values and an ellipti-

cal shape). The bright cloud nicknamed “Scooter” had a size of about 3° in latitude and 7.5° in longitude, and a variable shape. At a latitude of -41° , its size was about $3 \times 10^6 \text{ km}^2$. Other infrared-bright features that we observed on Sept. 6 (Fig. 1) and October 12 (Fig. 4) had sizes that we estimate to be $\leq 1 \times 10^8 \text{ km}^2$ and $\leq 1.5 \times 10^7 \text{ km}^2$, respectively. The size range we infer for the infrared-bright features therefore is similar to previous observations.

Although we are not able to model the haze column density in the bright features as we did for the clear atmosphere (due to the uncertainties in parameters such as the storm size and altitude), we can make an estimate of the storm altitude based on its appearance in the four filters. We conclude that the disturbance leading to infrared brightness must be located near or somewhat above the tropopause ($\simeq 0.1 \text{ bar}$). If it were located much

below this altitude it would not be seen in the 2.12- and 2.27- μm filters, where it appears very bright (compare Figs. 9b and 9c). However, the storm is unlikely to be high in the stratosphere; in this case its brightness would be similar in all four filters since it would be located above any other source of opacity.

5. CONCLUSIONS

We have presented results from observations of Neptune using both high-resolution speckle imaging at a resolution of 0.04'' and conventional imaging with narrowband filters. These two methods of observing the planet are complementary: the speckle data give information on the size, shape, and location of infrared-bright features, while the narrowband data allow us to model the vertical structure of Neptune's stratosphere, both within the bright features and in cloud-free regions.

The speckle data allow us to determine rotation periods for two storm features at $-45 \pm 8.5^\circ$ and $-30 \pm 8.5^\circ$ latitude, which are in good agreement with previous values. Our speckle images also give us an unprecedented resolution of 0.04'' at 2 μm , or about 60 resolution elements across the disk of Neptune. Future observations of bright features taken days or hours apart will allow us to track the evolution of these features in time, not only to obtain more accurate estimates of rotation periods, but also to track changes in spot shape or size.

We modeled the I/F measured in four narrowband wavelengths probing different altitudes in Neptune's atmosphere using a single thin haze layer; our result for the column density of this haze layer is $\simeq 10^7 \text{ cm}^{-2}$ if the haze is located around 0.3 bar. We consider this solution to be unlikely based on what is known of Neptune's cloud layers. We have therefore proposed a second solution, consisting of a haze layer of $\simeq 10^6 \text{ cm}^{-2}$ at $P < 0.05$ bars plus a second haze layer at ≥ 0.6 bar.

Estimates of the size of the brightest storm features in our data suggest that they are similar in size to the large storms that have been previously detected (e.g., the Great Dark Spot or the storm we observed in our high-resolution speckle images on Sept. 6 1996). It is clear from the models that the storm is located in the lower stratosphere, near the tropopause; whether it extends down into the troposphere cannot be inferred from the data. Based upon the research described in this paper we believe that further progress in atmospheric modeling of storm systems requires the use of high spatial resolution imaging in narrowband filters. This cannot be obtained with speckle imaging (Neptune is not bright enough to allow speckle imaging in narrowband filters), but requires the use of adaptive optics systems on large telescopes.

In the future observations of Neptune using adaptive optics at the Keck Telescope will allow us to observe Neptune at very high (diffraction limited) spatial resolution using narrowband filters; this will allow us to cleanly separate storm and quiescent atmosphere and to determine the sizes, shapes, and vertical extent of infrared-bright features to a greater accuracy than has been previously possible.

ACKNOWLEDGMENTS

This work was supported in part by NASA Grant NRA-97-OSS-04-98-053 (R3281). This work was also funded by a grant from the Lawrence Livermore Laboratory's Institute of Geophysics and Planetary Physics. This research was aided by a Grant-in-Aid of Research from the National Academy of Sciences, through Sigma Xi, The Scientific Research Society. This work has been supported in part by the National Science Foundation Science and Technology Center for Adaptive Optics, managed by the University of California at Santa Cruz under Cooperative Agreement AST 9876783.

Our thanks to Don Banfield and an anonymous reviewer who provided many helpful suggestions. This work was performed under the auspices of the U.S. Department of Energy, National Nuclear Security Administration, by the University of California, Lawrence Livermore National Laboratory under Contract W-7405-Eng-48.

REFERENCES

- Baines, K. H., and H. B. Hammel 1994. Clouds, hazes, and the stratospheric methane abundance in Neptune. *Icarus* **109**, 20–39.
- Baines, K. H., R. A. West, L. P. Giver, and F. Moreno 1993. Quasi-random narrow-band model fits to near-infrared low-temperature laboratory methane spectra and derived exponential-sum absorption coefficients. *J. Geophys. Res.* **98**, 5517–5529.
- Baines, K. H., H. B. Hammel, K. A. Rages, P. N. Romani, and R. E. Samuelson 1995. Clouds and hazes in the atmosphere of Neptune. In *Neptune and Triton* (D. P. Cruikshank, Ed.), pp. 489–546. Univ. of Arizona Press, Tucson.
- Belton, M. J. S., and R. J. Terrile 1984. Rotational properties of Uranus and Neptune. In *Uranus and Neptune* (J. T. Bergstralh, Ed.), pp. 327–347. NASA CP-2330.
- Borysow, A. 1991. Modeling of collision-induced infrared absorption spectra of H₂–H₂ pairs in the fundamental band at temperatures from 20 to 300 K. *Icarus* **92**, 273–279.
- Borysow, A. 1993. Erratum to: Rotovibrational collision-induced absorption spectra of H₂–H₂ pairs in the fundamental band (0 → 1) at temperatures from 20 to 300 K. *Icarus* **106**, 614.
- Borysow, A., and L. Frommhold 1989. Collision-induced infrared spectra of H₂–He pairs at temperatures from 18 to 7000 K II—overtone and hot bands. *Astrophysics J.* **341**, 549–555.
- Borysow, A., L. Frommhold, and M. Moraldi 1989. Collision-induced infrared spectra of H₂–He pairs involving 0–1 vibrational transitions and temperatures from 18 to 7000 K. *Astrophysics J.* **336**, 495–503.
- Cassali, M. 1992. A set of faint JHK standards for UKIRT. *UKIRT Newsletter* **4**, 33.
- Colina, L., R. C. Bohlin, and F. Castelli 1996. The 0.12–2.5 micron absolute flux distribution of the Sun for comparison with solar analog stars. *Astron. J.* **112**, 307–315.
- de Pater, I., P. N. Romani, and S. K. Atreya 1991. Possible microwave absorption by H₂S gas in Uranus' and Neptune's atmospheres. *Icarus* **91**, 220–233.
- Fink, U., and H. P. Larson 1979. The infrared spectra of Uranus, Neptune, and Titan from 0.8 to 2.5 microns. *Astrophys. J.* **233**, 1021–1040.
- Gibbard, S. G., B. Macintosh, D. Gavel, C. E. Max, I. de Pater, A. M. Ghez, E. F. Young, and C. P. McKay 1999. Titan: High resolution speckle images from the Keck Telescope. *Icarus* **139**, 189–201.
- Hammel, H. B. 1989. Discrete cloud structure on Neptune. *Icarus* **80**, 14–22.
- Hammel, H. B., and M. W. Buie 1987. An atmospheric rotation period of Neptune determined from methane-band imaging. *Icarus* **72**, 62–68.
- Hammel, H. B., and G. W. Lockwood 1997. Atmospheric structure of Neptune in 1994, 1995, and 1996: HST imaging at multiple wavelengths. *Icarus* **129**, 466–481.

- Hammel, H. B., K. H. Baines, and J. T. Bergstralh 1989a. Vertical aerosol structure of Neptune: Constraints from center-to-limb profiles. *Icarus* **80**, 416–438.
- Hammel, H. B., and 12 colleagues 1989b. Neptune's wind speeds obtained by tracking clouds in Voyager images. *Science* **245**, 1367–1369.
- Hammel, H. B., S. L. Lawson, J. Harrington, G. W. Lockwood, D. T. Thompson, and C. Swift 1992. An atmospheric outburst on Neptune from 1986 through 1989. *Icarus* **99**, 363–367.
- Hammel, H. B., G. W. Lockwood, J. R. Mills, and C. D. Barnet 1995. Hubble Space Telescope imaging of Neptune's cloud structure in 1994. *Science* **268**, 1740–1742.
- Ingersoll, A. P., C. D. Barnet, R. F. Beebe, F. M. Flasar, D. P. Hinson, S. S. Limaye, L. A. Sromosky, and V. E. Suomi 1995. Dynamic meteorology of Neptune. In *Neptune and Triton* (D. P. Cruikshank, Ed.), pp. 613–682. Univ. of Arizona Press, Tucson.
- Irwin, P. G. J., S. B. Calcutt, F. W. Taylor, and A. L. Weir 1996. Calculated k distribution coefficients for hydrogen- and self-broadened methane in the range 2000–9500 cm^{-1} from exponential sum fitting to band-modelled spectra. *J. Geophys. Res.* **101**, 26137–26154.
- Joyce, R. R., C. B. Pilcher, D. P. Cruikshank, and D. Morrison 1977. Evidence for weather on Neptune. *Astrophys. J.* **214**, 657–662.
- Limaye, S. S., and L. A. Sromovsky 1991. Winds of Neptune: Voyager observations of cloud motions. *J. Geophys. Res.* **96**, 18941–18960.
- Lindal, G. F. 1992. The atmosphere of Neptune: An analysis of radio occultation data acquired with Voyager 2. *Astron. J.* **103**, 967–982.
- Lockwood, G. W., D. T. Thompson, H. B. Hammel, P. Birch, and M. Candy 1991. Neptune's cloud structure in 1989: Photometric variations and correlation with ground-based images. *Icarus* **90**, 299–307.
- Massie, S. T., and D. M. Hunten 1982. Conversion of para and ortho hydrogen in the jovian planets. *Icarus* **49**, 213–226.
- Matthews, K., and B. T. Soifer 1994. *Infrared Astronomy with Arrays: The Next Generation* (I. McLean, Ed.). Kluwer Academic, Dordrecht, p. 239.
- Matthews, K., A. M. Ghez, A. J. Weinberger, and G. Neugebauer 1996. The first diffraction-limited images from the W. M. Keck Telescope. *Publications of the Astronomical Society of the Pacific* **108**, 615–619.
- Moses, J. I., M. Allen, and Y. L. Yung 1992. Hydrocarbon nucleation and aerosol formation in Neptune's atmosphere. *Icarus* **99**, 318–346.
- Moses, J. I., K. Rages, and J. B. Pollack 1995. An analysis of Neptune's stratospheric haze using high-phase-angle Voyager images. *Icarus* **113**, 232–266.
- Orton, G. S., J. H. Lacy, J. M. Achtermann, P. Parmer, and W. E. Blass 1992. Thermal spectroscopy of Neptune—The stratospheric temperature, hydrocarbon abundances, and isotopic ratios. *Icarus* **100**, 541–555.
- Persson, S. E., D. C. Murphy, W. Krzeminski, M. Roth, and M. J. Rieke 1998. A new system of faint near-infrared standard stars. *Astrophysics J.* **116**, 2475.
- Pilcher, C. B. 1977. Evidence for weather on Neptune II. *Astrophys. J.* **214**, 663–666.
- Pryor, W. R., R. A. West, K. E. Simmons, and M. Delitsky 1992. High-phase-angle observations of Neptune at 2650 Å and 7500 Å: Haze structure and particle properties. *Icarus* **99**, 302–317.
- Roddier, F., C. Roddier, A. Brahic, C. Dumas, J. E. Graves, M. J. Northcott, and T. Owen 1997. First ground-based adaptive optics observations of Neptune and Proteus. *Planet. Space Sci.* **45**, 1031–1036.
- Roddier, F., C. Roddier, J. E. Graves, M. J. Northcott, and T. Owen 1998. NOTE: Neptune's cloud structure and activity: Ground-based monitoring with adaptive optics. *Icarus* **136**, 168–172.
- Romani, P. N., and S. K. Atreya 1989. Stratospheric aerosols from CH₄ photochemistry on Neptune. *Geophys. Res. Lett.* **16**, 941–944.
- Romani, P. N., J. Bishop, B. Bezard, and S. Atreya 1993. Methane photochemistry on Neptune: Ethane and acetylene mixing ratios and haze production. *Icarus* **106**, 442–463.
- Smith, B. A., and 64 colleagues 1989. Voyager 2 at Neptune: Imaging science results. *Science* **246**, 1422–1449.
- Sromovsky, L. A., S. S. Limaye, and P. M. Fry 1993. Dynamics of Neptune's major cloud features. *Icarus* **105**, 110–141.
- Sromovsky, L. A., S. S. Limaye, and P. M. Fry 1995. Clouds and circulation on Neptune: Implications of 1991 HST observations. *Icarus* **118**, 25–38.
- Sromovsky, L. A., P. M. Fry, K. H. Baines, S. S. Limaye, G. S. Orton, and T. E. Dowling 2001a. Coordinated 1996 HST and IRTF imaging of Neptune and Triton. I. Observations, navigation, and differential deconvolution. *Icarus* **149**, 416–434.
- Sromovsky, L. A., P. M. Fry, K. H. Baines, and T. E. Dowling 2001b. Coordinated 1996 HST and IRTF imaging of Neptune and Triton. II. Implications of disk-integrated photometry. *Icarus* **149**, 435–458.
- Sromovsky, L. A., P. M. Fry, T. E. Dowling, K. H. Baines, and S. S. Limaye 2001c. Coordinated 1996 HST and IRTF imaging of Neptune and Triton. III. Neptune's atmospheric circulation and cloud structure. *Icarus* **149**, 459–288.
- West, R. A., D. F. Strobel, and M. G. Tomasko 1986. Clouds, aerosols and photochemistry in the jovian atmosphere. *Icarus* **65**, 161–217.
- Zheng, C., and A. Borysow 1995. Modeling of collision-induced infrared absorption spectra of H₂ pairs in the first overtone band at temperatures from 20 to 500 K. *Icarus* **113**, 84–90.